

A Se vacancy induced localized Raman mode in two-dimensional MoSe₂ grown by CVD

Shudong Zhao^{1,‡}, Meilin Lu^{1,‡}, ShaSha Xue¹, Lin Yan¹, Peng Miao², Yan Hang³, Xianjie Wang¹, Zhiguo Liu¹, Yi Wang⁴, Lei Tao⁵, Yu Sui¹ and Yang Wang⁴

¹ Department of Physics, Harbin Institute of Technology, Harbin 150001, People's Republic of China.

² School of Chemistry and Chemical Engineering, Harbin Institute of Technology, Harbin 150001, People's Republic of China.

³ School of Materials Science and Engineering, Harbin Institute of Technology, Harbin 150001, People's Republic of China

⁴ Academy of Fundamental and Interdisciplinary Sciences, Harbin Institute of Technology, Harbin 150001, People's Republic of China.

⁵ Laboratory for Space Environment and Physical Sciences, Harbin Institute of Technology, Harbin 150001, People's Republic of China

‡ Shudong Zhao and Meilin Lu contributed equally to this work

E-mail: taolei@hit.edu.cn (Lei Tao); suiyu@hit.edu.cn (Yu Sui); yangwang@hit.edu.cn (Yang Wang)

Abstract

Defects play a significant role in optical properties of semiconducting two-dimensional transition metal dichalcogenides (TMDCs). In ultra-thin MoSe₂, a remarkable feature at ~ 250 cm⁻¹ in Raman spectra is ascribed to be a defect-related mode. Recent attempts failed to explain the origin of this peak, leaving it being a mystery. Here in this work, we demonstrate that this peak is a Se vacancy induced defect mode. Heat effect and hydrogen etching are two main factors to introduce Se vacancies in CVD process of growing MoSe₂. A phonon confinement model can well explain the behaviors of intrinsic Raman modes. Density functional theory (DFT) calculation reveals that single Se vacancy (V_{Se}) is responsible for the appearance of Raman peak at ~ 250 cm⁻¹ and this mode is an A_{1g}-like localized mode which is also confirmed by polarized Raman scattering experiment. The relative strength of this mode can be a characterization of the quality of 2D MoSe₂. This work may offer a simple method to tailor chalcogenide vacancies in 2D TMDCs and provide a way to study their vibrational properties.

Keywords: MoSe₂, Se vacancy, defect-induced Raman mode, local mode

1. Introduction

Two-dimensional (2D) transition metal dichalcogenides (TMDCs), in particular MoS₂, MoSe₂, WS₂ and WSe₂, have shown novel properties in many aspects, such as direct-bandgap nature at monolayer scale^{1,2}, large exciton binding energy^{3,4}, large carrier mobility^{5,6}, valley polarization⁷, room-temperature ferromagnetism⁸ and so on. These properties make 2D TMDCs a kind of very promising material for applications in electronic, optoelectronic, valley electronics or spintronic devices. Although great achievements have been made in field effect transistors^{6, 9-11}, light-emitting diodes¹², CMOS or large-scale integrated circuits^{13, 14}, some fundamental physics of these materials are still less known, especially in structure of defects and roles of defects in electrical, magnetic or optical properties of 2D TMDCs. Recently, structure of defects in TMDCs have been characterized by STEM and STM measurement. However, these two methods are expensive and have strict requirements on sample, which may even cause damages of the ultra-thin TMDCs in process of sample preparation or electron irradiation^{15, 16}.

Raman spectrum has been proved to be a fast, convenient and non-destructive method to characterize the defects in 2D TMDCs. Previously in MoS₂ and WS₂, defects has been proved to lead to shifting of characteristic peaks and appearance of new defect-related peaks in Raman spectra¹⁷⁻¹⁹. As to MoSe₂, except two main features of Raman scattering, peak ~ 240 cm⁻¹ for A_{1g} mode and peak ~ 288 cm⁻¹ for E_{2g}¹ mode²⁰, a remarkably mysterious peak around 250 cm⁻¹ may or may not show in Raman spectra of the as-prepared samples, obtained by either exfoliation or CVD methods as far as our best survey is concerned²¹⁻³⁶. Moreover, its relative intensity varies in different works, so it is reasonable to draw a clue that this unknown peak is related to the quality of the MoSe₂ nanosheets synthesized by different methods in different research groups. Nevertheless, the assignment of this peak is still controversial.

Recently, in Ismail's work the Raman peak at 250 cm⁻¹ was assigned to the double resonance of ZA mode at M point Brillouin zone that appears in high-quality thin MoSe₂ films using MoO₂ powders instead of MoO₃ as precursor³⁶. But in general, the appearance of a new peak in Raman spectra is usually associated with some kind of lattice disorder. As reported in Masoud's work, the peak at 250 cm⁻¹ is associated with Se vacancies which are introduced by laser heating in their laser-based synthesis approach. STEM results confirmed two structures of Se vacancies, i.e. single Se vacancy (V_{Se}) and dual Se column vacancy (V_{2Se}). However, their density functional theory (DFT) calculation results failed to assign this peak using the supercells with different V_{Se} concentrations³⁷.

Here, in order to make sure what cause Se vacancies in CVD prepared 2D MoSe₂ and what structure of Se vacancy is and how Se vacancy induces this mysterious peak at ~250 cm⁻¹ in Raman spectrum, we adopted CVD method using MoO₃ and Se powders as precursors like most other works did to synthesize MoSe₂ nanosheets^{21, 29}. We found that growth temperature and the flow rate of hydrogen are two key factors influence the vibrational properties of CVD-grown MoSe₂. In sample grown at higher growth temperature and with higher hydrogen flow rate, a new peak emerges at ~250 cm⁻¹ and strengthens, which demonstrates that Se vacancies can be introduced by thermal annealing and hydrogen etching in CVD processing. DFT calculation results are in good agreement with the experiment data and indicate that the defect-related mode at 250 cm⁻¹ is an A_{1g}-like localized mode bounded to V_{Se}, which is confirmed by polarized Raman scattering experiments. Our findings solve a long-standing problem in literature and

invalidate recent attempts to assign this peak in 2D MoSe₂^{27, 34, 36-38}. And our methods can be extended to other kind of 2D TMDCs or TMDCs alloys to study their vibrational properties.

2. Methods

Sample preparations: The CVD processes to synthesize MoSe₂ nanosheets is like our previous work to grown WSe₂³⁹. To tailor the Se vacancies, the growth temperature and the flow rate of hydrogen were tuned. The total flow rate of Ar and H₂ was kept at the fixed value of 58 sccm.

Raman scattering measurements: The normal Raman spectra and mappings were performed in a Renishaw inVia Raman microscope equipped with a 532 nm laser. Polarized Raman scattering measurements were performed in a NT-MDT NTEGRA Spectra Raman system with 532 nm excitation (See Figure S6).

Density functional theory (DFT) calculations: Vibrational and Raman properties were calculated by Vienna ab initio simulation package (VASP) using the projector-augmented wave (PAW) methods and Perdew-Burke-Ernzerhof (PBE) functional with D3 correction (DFT-D3). Three different V_{Se} concentrations (pristine, 11.1% and 25%) were concerned (see details in Supporting Information).

2. Results and discussions

2.1 Heating effect and hydrogen etching in CVD process

MoSe₂ monolayers are synthesized by CVD method as most works utilized, with MoO₃ and Se powders being the precursors (see details in Experimental section). Figure 1(a) shows the optical image of a MoSe₂ monolayer with a second layer at the central area, identified by the PL spectra (insert). Raman spectra and Raman intensity mapping image at 351 cm⁻¹ (B¹_{2g} mode in multilayer) in Figure 1(b) also confirm it. Except for the A_{1g} mode at ~239 cm⁻¹ and E¹_{2g} mode at ~288 cm⁻¹, a remarkable peak located at about 250 cm⁻¹ is also commonly found in our CVD grown MoSe₂ nanosheets. This peak has been proved to be a Se vacancy defect-activated mode by Masoud et al³⁷. In their work, the losses of Se in the MoSe₂ powder precursors are mainly caused by the laser heating during the first 2 minutes of their laser-based synthesis process. We conjecture the heat etching effect also exists in CVD procedures. In another hand, a small amount of hydrogen is always introduced in reducing MoO₃ reaction. The hydrogen may react with the just grown MoSe₂ nanosheets during growth and cooling procedure. Similar effect of hydrogen etching can be traced in CVD processing of graphene growth⁴⁰.

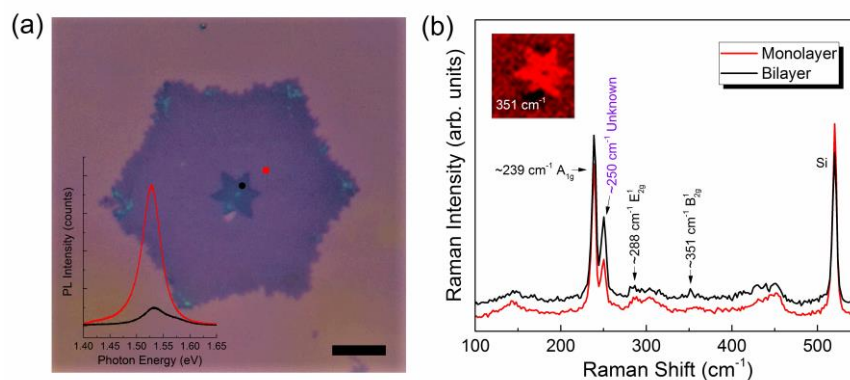


Figure 1 (a) Optical image and PL spectra of as prepared a MoSe₂ nanosheet. Scale bar is 10 μm . (b) Raman spectra of the monolayer and the bilayer MoSe₂. Insert is the Raman mapping image at the bilayer region

So we designed experiments using four different parameters. The correlated Raman results are

illustrated in Figure 2. With higher growth temperature and higher flow rate of hydrogen, the relative intensity of peak D (defect-related peak around 250 cm^{-1}) to peak A_{1g} increases. Besides, peak A_{1g} weakens, shifts from 239.4 cm^{-1} to 234.1 cm^{-1} , and D peak has a slightly blue shift from 250 cm^{-1} to 253 cm^{-1} . These results show a good agreement with the experimental results in Masoud et al.'s work³⁷. So we successfully tailored the Se vacancy concentrations by CVD method, and found that growth temperature and the flow rate of hydrogen are two key factors inducing Se vacancies in CVD process of synthesizing MoSe_2 nanosheets. In addition, the etching effects of heating and hydrogen can also be confirmed by the Raman mapping images of a MoSe_2 monolayer shown in Figure 3.

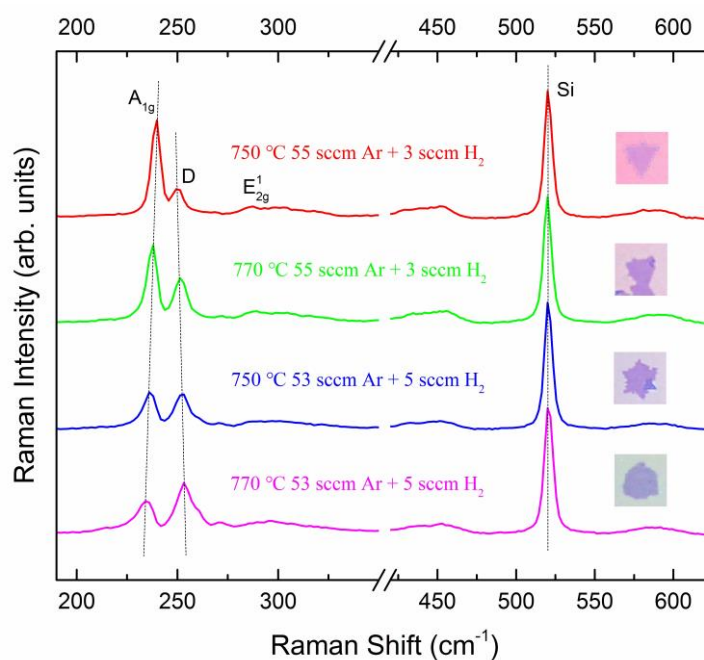


Figure 2 Raman spectra of MoSe_2 monolayers prepared by CVD at different growth parameters. The notations of the Raman peaks used here are same with that in Figure 1 for simplicity.

Figure 3(a) and Figure 3(b) exhibit the Raman intensity mapping images of A_{1g} and D peaks. Good homogeneity can be seen all over the monolayer except for the edge area, since it cannot be totally irradiated by laser spot ($\sim 1\text{ }\mu\text{m}$ diameter). Figure 3(c) and 3(d) show the variation of Raman intensity ratio between of A_{1g} and D modes. From center to edge, the ratio gradually turns smaller, i.e. the central areas of the nanosheets have larger amount of defects. In WS_2 CVD synthesis processes reported in some previous works, similar etching mechanism was also discovered, that is the photoluminescence intensity gradually changes from center region to edge of the triangle WS_2 single layer⁴¹. It means that etching is concomitant with the growth of the crystal. Furthermore, it may also happen at the cooling procedure. As seen in atomic force microscope (AFM) images in Figure S1, the MoSe_2 nanosheet degrades about 800 nm and some nanoparticles regrow around the edges, as the same reversible reaction mechanism during cooling stage as reported by Bo Li et al⁴². Meanwhile, some vacant triangular or rhombic areas induced by etching can be seen clearly in the AFM phase image. So in order to avoid these etching effects in CVD processing, we used less hydrogen flow rate (2 sccm) and opened the furnace immediately after growth for fast cooling, then the D peak almost disappeared as shown in Figure S2.

Ismail et al. attributed the disappearing of D peak (assigned to $2Z\text{A(M)}$ in their work) to the degradation of the high-quality crystal after aging 6 months³⁶. However, in our work, due to the Se vacancies, the samples are quite unstable even under a vacuum environment, according to the

concentration of Se vacancies. The samples with high vacancy concentration are damaged after two month's aging, while the samples with low vacancy concentration remain unchanged (see Figure S3). Recently, when preparing our manuscript, the similar etching effect of hydrogen was also discovered in MoS₂ grown by chemical vapor deposition for photoluminescence enhancement⁴³. It indicates that this approach can be extended to all other TMDCs for a wide range of physical property studies.

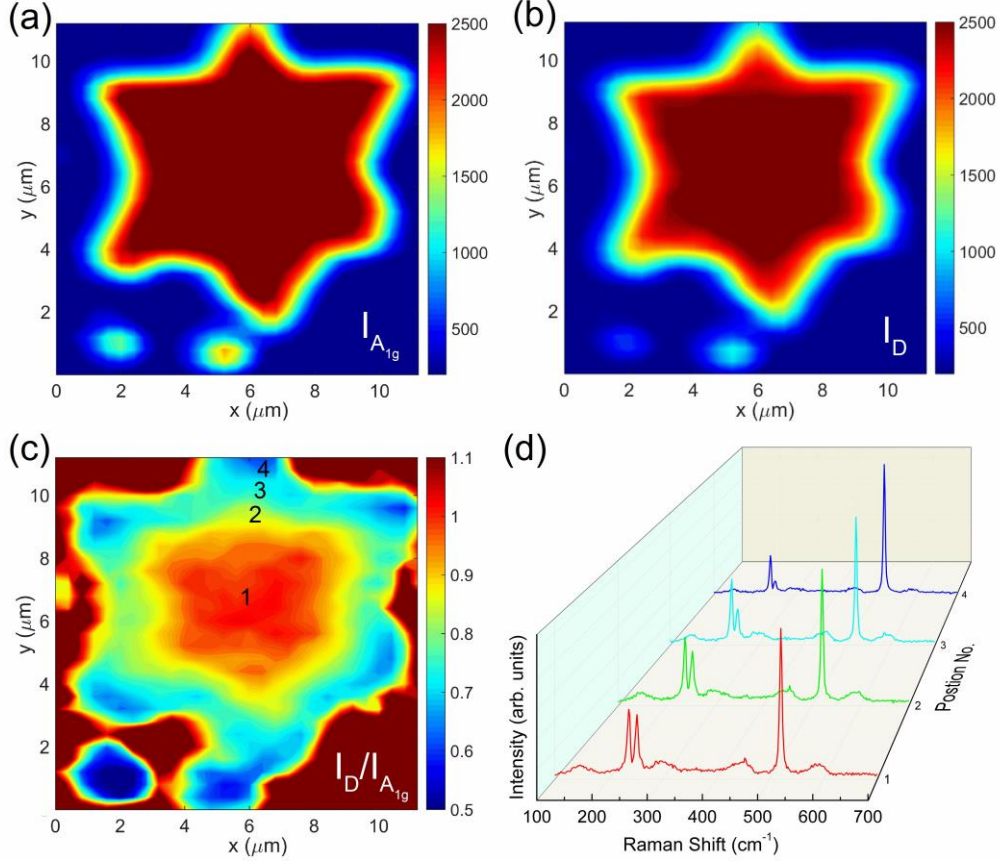


Figure 3 (a) Raman intensity mapping image of A_{1g} mode. (b) Raman intensity mapping image of D mode. (c) The intensity ratio mapping image of D mode to A_{1g} mode. (d) Four Raman spectra at different locations of the MoSe₂ monolayer as denoted in (c).

2.2 Behaviours of A_{1g} and E_{2g}¹ modes

It can be seen in Figure 2 that as Se vacancy concentration increases, except the down shifting, A_{1g} mode also shows an asymmetric broadening to lower wavenumber, while E_{2g}¹ mode seems unchanged. Previously, slight up shift of A_{1g} mode and down shift of E_{2g}¹ mode were observed in MoS₂⁴³, but both A_{1g} mode and E_{2g}¹ mode in WS₂ show down shift⁴⁴. We found that their behaviors with increasing defect concentrations follow the trend of their phonon dispersion when the wave vector gets away from Brillouin zone center point. It means that the phonons around Brillouin zone center or at Brillouin zone edge participate in the Raman process. A phonon confinement model can well explain the evolution of these two first-order optical phonon modes⁴⁵. The phonon dispersion of monolayer MoSe₂ is shown in Figure S5, the two branches of E_{2g}¹ mode, LO and TO phonon bands are relatively flat throughout the Brillouin zone, which agrees well with the behavior of E_{2g}¹ mode in Raman spectra. The A_{1g} phonon band shows obvious down shift along Γ -K and Γ -M. We calculated the line shapes of A_{1g} mode at different vacancy concentrations using the RWL model developed by Tan et al⁴⁴. The Se vacancy concentrations of all samples are characterized by X-ray photoelectron spectroscopy (see Figure S7).

Simulation results are presented in Figure 4, L_D means the grain size or the average distance between defects. As we can see, the line shapes and peak frequency shifts of A_{1g} mode are well fitted at all Se vacancy concentrations, except the additional Se vacancy-induced peak at $\sim 250 \text{ cm}^{-1}$. In addition, at 8% and 14% Se vacancy concentrations, there is another peak at around 215 cm^{-1} . According to the phonon dispersion, 215 cm^{-1} is just corresponding to the frequency of $A_{1g}(M)$, so it can be assigned to the $A_{1g}(M)$ due to the phonon confinement effect.

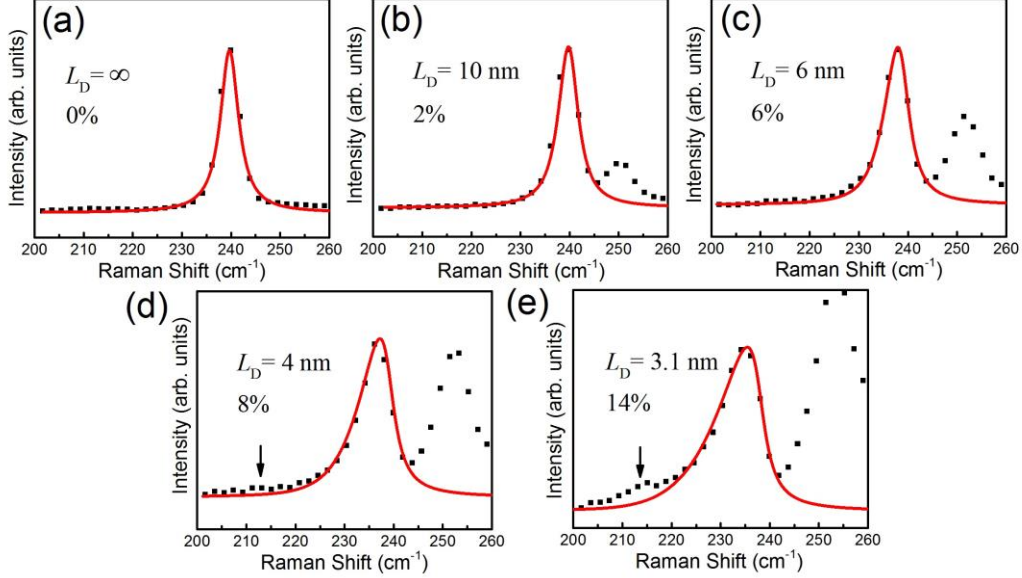


Figure 4 Simulation results of Raman spectra at (a) 0%, (b) 2%, (c) 6%, (d) 8% and (e) 14% Se vacancy concentrations. The corresponding fitting parameters L_D are (a) ∞ , (b) 10 nm, (c) 6 nm, (d) 4 nm and (e) 3.1 nm. All fitting parameters α is 0.008. Red line represents the calculated Raman curve and black symbol represents the experimental data.

2.3 DFT calculation of A_{1g} and D modes

So far we have demonstrated that growth temperature and flow rate of hydrogen are two key factors that can introduce and tailor Se vacancies in CVD grown MoSe_2 nanosheets. Besides, simulation results based on phonon confinement model give a perfect explanation on behaviors of intrinsic peaks of monolayer MoSe_2 with increasing Se vacancy concentrations. However it can not predict the new defect-activated peak in Raman spectra. In Masoud et al.'s work, both single Se vacancy (V_{Se}), and the column Se vacancy (V_{Se}) were detected by Z-contrast STEM³⁷. However, they failed to have a deep understanding of the single Se vacancy-activated Raman peak observed in experiments using density functional theory (DFT) calculation. No peak appeared at $\sim 250 \text{ cm}^{-1}$ in their calculated Raman spectra. So in order to confirm this Se vacancy defect type and to give a better understanding of this defect-related mode, we also utilized DFT simulations and three different V_{Se} concentrations were considered, i.e. 0% (pristine), 11.1% and 25% (see details in Supporting Information). With a Se atom removed from the lattice, the symmetry of MoSe_2 film becomes lower and more vibrational modes appear at the Brillouin zone center. Among all of these complicated vibrational modes, we can easily distinguish the A_{1g} mode from others by analyzing the vibrational images of the Raman modes.

Figure 5 shows the vibrational images of A_{1g} mode at different vacancy concentrations. The atomic vibration of A_{1g} mode in pure, perfect MoSe_2 monolayer is that Mo atomic layer is stationary while the bottom and top layers of Se atoms vibrate in opposite directions along z axis. Briefly, in defective samples the general behavior of the two layers of Se atoms remain unchanged, except that the vibration directions

of some Se atoms show different degrees of deviation to z axis, and Mo atoms participate in the vibration. This can be seen more clearly in the animation of this vibrational mode (A_{1g} 11.1%.mp4).

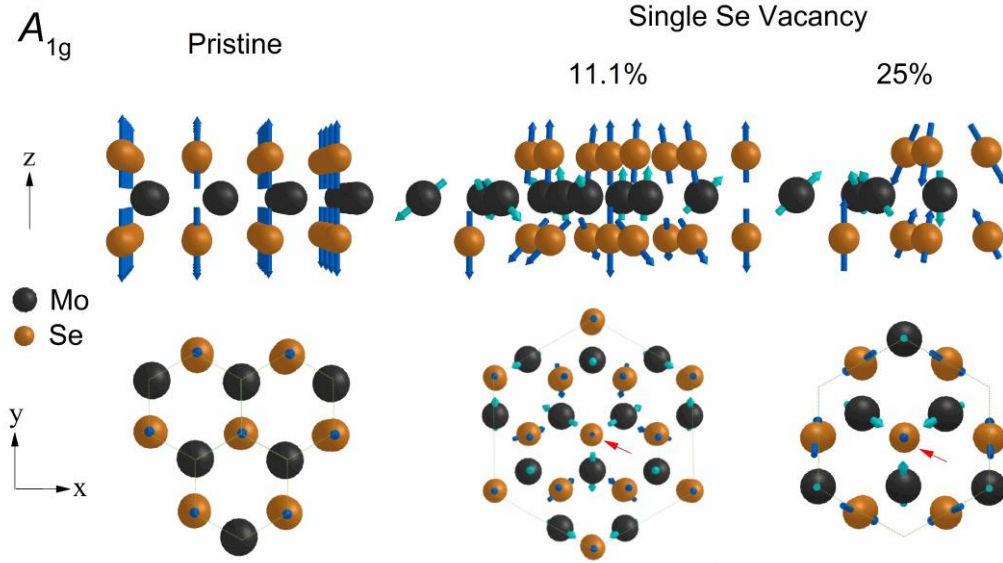


Figure 5 Vibrational images of A_{1g} mode at different V_{Se} concentrations. The upper line are the side views along z axis, the bottom line are the top views. The green hexagonal line means one unit cell. The red arrows point to the locations of V_{Se} .

In detail, after removing a top Se atom from the lattice, the unit cell remains to be hexagonal but centered by the Se vacancy. The Se atom under the V_{Se} still vibrates along z axis. The motions of the six nearest neighbor bottom Se atoms are affected most in 11.1% vacancy sample. At a further distance, the twelve second nearest neighbor Se atoms are not affected. As in the 25% vacancy sample, all neighbor Se atoms are influenced by the Se vacancy because the distances between Se vacancies are shorter at higher vacancy concentrations. These variations of motions of Mo atoms and Se atoms can be directly related to red shift of A_{1g} mode. As shown in the calculated Raman spectra in Figure 6(a), the frequency of A_{1g} mode is decreased by 16 cm^{-1} from 0% to 25%. The calculated phonon frequency shift of A_{1g} shows highly agreement of previous work³⁷.

Now we focus on the defect related mode. As seen in Figure 6(a), except for the red-shifted A_{1g} mode, a defect induced peak emerges at $\sim 254\text{ cm}^{-1}$ at 11.1% vacancy concentration and it shifts to 260 cm^{-1} when the concentration increases to 25%. We assign it to the D mode. The calculated Raman spectra show great agreement with our experimental results, except the strength of D mode is underestimated. We extract the vibrational images and Raman tensors of D mode. As shown in Figure 6(b), D mode is also an out-of-plane mode and the vibrational behavior of D mode is quite similar with A_{1g} mode in defective samples. The main difference between D mode and A_{1g} mode is that the vibrational direction of the Se atom under the vacancy is opposite with other Se atoms in the bottom layer. Another distinct feature is that, at 11.1% V_{Se} concentration, the three nearest Mo atoms of V_{Se} and the Se atoms have much larger vibrational amplitude. At the six corners of unit cell, the amplitude of bottom Se atoms becomes smaller and the six top Se atoms are static due to longer distance from the V_{Se} (see more clearly in D 11.1%. mp4). This is a typical picture of local mode⁴⁶, indicating that D mode may be the localized A_{1g} mode bounded to V_{Se} . Surprisingly, the D mode has the same form of Raman tensor with A_{1g} mode⁴⁷. Our calculations can well explain the correlation between D mode and A_{1g} mode discovered by previous works^{34,36}.

To further confirm this, polarized Raman spectra of samples at three different Se vacancy

concentrations are collected. As shown in Figure 6(c), at cross configuration, the A_{1g} peak nearly disappears while E_{2g}^1 peak remains unchanged which highly consist with theoretical analysis and experimental results in other works^{48,49}. The D peak also disappears at cross configuration. Additionally, Figure 6(d) illustrates the polar plots of Raman intensity as function of the polarized direction of incident light. As expected, the line shape of A_{1g} mode shows a typical dumbbell structure as previous works found⁴⁸. D mode has the same structure which agrees very well with our calculation results.

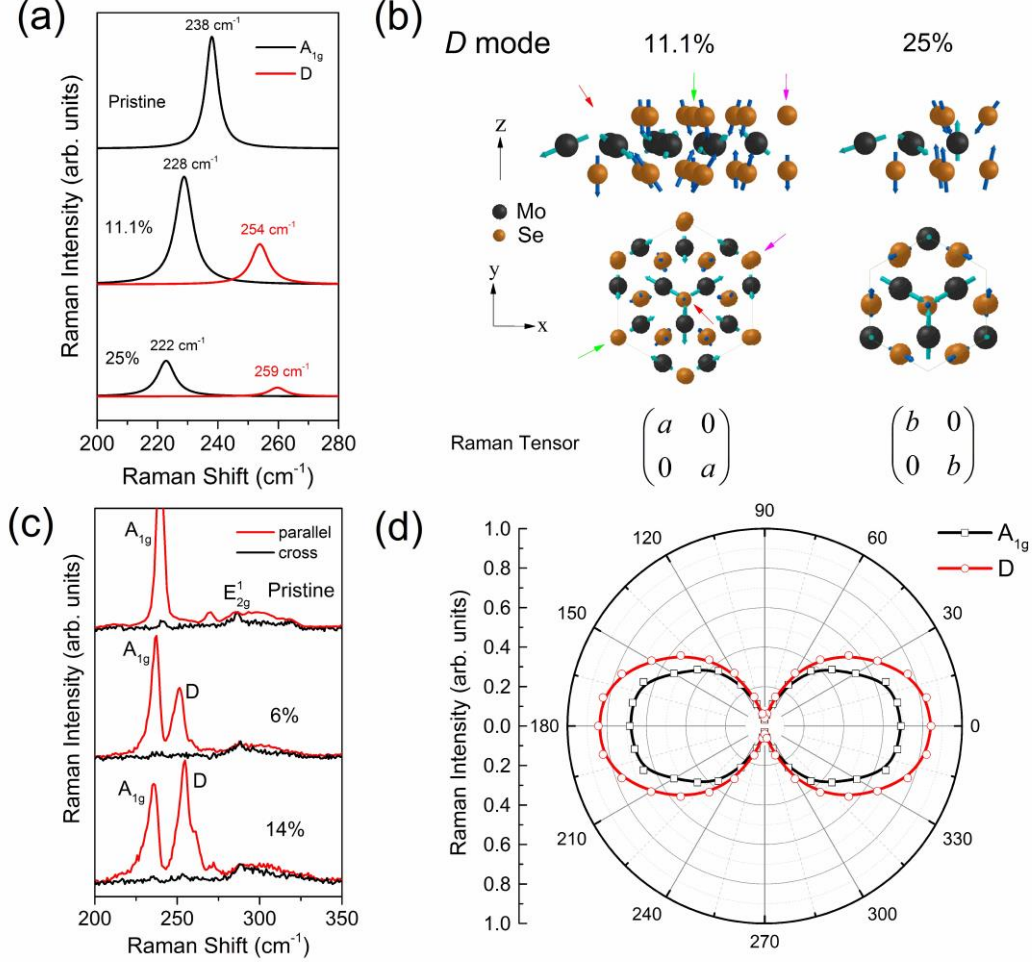


Figure 6 Calculated Raman spectra of MoSe₂ at different VSe concentrations. (b) The vibrational images and Raman tensor of D modes at 11.1% and 25% V_{Se}. Red arrows point to the V_{Se}, green and magenta arrows point to the two unequivalent sites at corners of the hexagonal unit cell. (c) Polarized Raman spectra of three MoSe₂ sample with 0%, 6% and 14% VSe concentrations. (d) Polar plot of the Raman intensity as a function of ϕ for A_{1g} and D modes.

3. Conclusions

In summary, using CVD methods we have successfully tailored the concentrations of Se vacancies in two-dimensional MoSe₂ through tuning the growth temperature and flow rate of hydrogen. The characteristic A_{1g} peak of MoSe₂ in the Raman spectra shifts to lower energy and a new peak (labelled as D) at ~ 250 cm⁻¹ emerges and shows a little blue shift with increasing Se vacancy concentrations. DFT calculations demonstrated that D peak originates from single Se vacancy and it is an A_{1g} -like out-of-plane vibrational mode localized to the single Se vacancy. The polarized Raman spectra confirmed our calculation results. Our findings may pave a way to tailor the chalcogenide element vacancies in two-

dimensional TMDCs by CVD method, and to investigate their vibrational properties with defects.

Supporting information

Supporting Information is available from the Wiley Online Library or from the author.

Acknowledgements

This research was financially supported by the National Natural Science Foundation of China (No. 11304060) and the Foundation of Harbin Institute of Technology for the Incubation Program of the development of basic research outstanding talents (No. 01509321) and the China Postdoctoral Science Foundation.

References

1. Mak, K. F.; Lee, C.; Hone, J.; Shan, J.; Heinz, T. F. *J. Phys. Rev. Lett.*, Atomically thin MoS₂: a new direct-gap semiconductor. **2010**, *105* (13), 136805.
2. Splendiani, A.; Sun, L.; Zhang, Y.; Li, T.; Kim, J.; Chim, C.-Y.; Galli, G.; Wang, F. *J. Phys. Rev. Lett.*, Emerging photoluminescence in monolayer MoS₂. **2010**, *10* (4), 1271-1275.
3. Mak, K. F.; He, K.; Lee, C.; Lee, G. H.; Hone, J.; Heinz, T. F.; Shan, J. *J. Phys. Chem. Lett.*, Tightly bound trions in monolayer MoS₂. **2013**, *12* (3), 207.
4. You, Y.; Zhang, X.-X.; Berkelbach, T. C.; Hybertsen, M. S.; Reichman, D. R.; Heinz, T. F. *J. Phys. Rev. Lett.*, Observation of biexcitons in monolayer WSe₂. **2015**, *11* (6), 477.
5. Kaasbjerg, K.; Thygesen, K. S.; Jauho, A.-P. *J. Phys. Rev. B*, Acoustic phonon limited mobility in two-dimensional semiconductors: Deformation potential and piezoelectric scattering in monolayer MoS₂ from first principles. **2013**, *87* (23), 235312.
6. Radisavljevic, B.; Radenovic, A.; Brivio, J.; Giacometti, I.; Kis, A. *J. Phys. Chem. Lett.*, Single-layer MoS₂ transistors. **2011**, *6* (3), 147.
7. Zeng, H.; Dai, J.; Yao, W.; Xiao, D.; Cui, X. *J. Phys. Chem. Lett.*, Valley polarization in MoS₂ monolayers by optical pumping. **2012**, *7* (8), 490.
8. Tao, L.; Meng, F.; Zhao, S.; Song, Y.; Yu, J.; Wang, X.; Liu, Z.; Wang, Y.; Li, B.; Wang, Y. *J. Phys. Chem. Lett.*, Experimental and theoretical evidence for the ferromagnetic edge in WSe₂ nanosheets. **2017**, *9* (15), 4898-4906.
9. Zhang, Y.; Ye, J.; Matsushashi, Y.; Iwasa, Y. *J. Phys. Chem. Lett.*, Ambipolar MoS₂ thin flake transistors. **2012**, *12* (3), 1136-1140.
10. Perera, M. M.; Lin, M.-W.; Chuang, H.-J.; Chamlagain, B. P.; Wang, C.; Tan, X.; Cheng, M. M.-C.; Tománek, D.; Zhou, Z. *J. Phys. Chem. Lett.*, Improved carrier mobility in few-layer MoS₂ field-effect transistors with ionic-liquid gating. **2013**, *7* (5), 4449-4458.
11. Das, S.; Chen, H.-Y.; Penumatcha, A. V.; Appenzeller, J. *J. Phys. Chem. Lett.*, High performance multilayer MoS₂ transistors with scandium contacts. **2012**, *13* (1), 100-105.
12. Ponomarev, E.; Gutiérrez-Lezama, I.; Ubrig, N.; Morpurgo, A. F. *J. Phys. Chem. Lett.*, Ambipolar light-emitting transistors on chemical vapor deposited monolayer MoS₂. **2015**, *15* (12), 8289-8294.
13. Radisavljevic, B.; Whitwick, M. B.; Kis, A. *J. Phys. Chem. Lett.*, Integrated circuits and logic operations based on single-layer MoS₂. **2011**, *5* (12), 9934-9938.
14. Wang, H.; Yu, L.; Lee, Y.-H.; Shi, Y.; Hsu, A.; Chin, M. L.; Li, L.-J.; Dubey, M.; Kong, J.; Palacios, T. *J. Phys. Chem. Lett.*, Integrated circuits based on bilayer MoS₂ transistors. **2012**, *12* (9), 4674-4680.

15. Zan, R.; Ramasse, Q. M.; Jalil, R.; Georgiou, T.; Bangert, U.; Novoselov, K. S. J. A. n., Control of radiation damage in MoS₂ by graphene encapsulation. **2013**, *7* (11), 10167-10174.
16. Komsa, H.-P.; Kotakoski, J.; Kurasch, S.; Lehtinen, O.; Kaiser, U.; Krasheninnikov, A. V. J. P. r. l., Two-dimensional transition metal dichalcogenides under electron irradiation: defect production and doping. **2012**, *109* (3), 035503.
17. Bae, S.; Sugiyama, N.; Matsuo, T.; Raebiger, H.; Shudo, K.-i.; Ohno, K. J. P. R. A., Defect-induced vibration modes of Ar⁺-irradiated MoS₂. **2017**, *7* (2), 024001.
18. Lee, C.; Jeong, B. G.; Yun, S. J.; Lee, Y. H.; Lee, S. M.; Jeong, M. S. J. A. n., Unveiling Defect-Related Raman Mode of Monolayer WS₂ via Tip-Enhanced Resonance Raman Scattering. **2018**, *12* (10), 9982-9990.
19. Parkin, W. M.; Balan, A.; Liang, L.; Das, P. M.; Lamparski, M.; Naylor, C. H.; Rodríguez-Manzo, J. A.; Johnson, A. C.; Meunier, V.; Drndić, M. J. A. n., Raman shifts in electron-irradiated monolayer MoS₂. **2016**, *10* (4), 4134-4142.
20. Tonndorf, P.; Schmidt, R.; Böttger, P.; Zhang, X.; Börner, J.; Liebig, A.; Albrecht, M.; Kloc, C.; Gordan, O.; Zahn, D. R. J. O. e., Photoluminescence emission and Raman response of monolayer MoS₂, MoSe₂, and WSe₂. **2013**, *21* (4), 4908-4916.
21. Wang, X.; Gong, Y.; Shi, G.; Chow, W. L.; Keyshar, K.; Ye, G.; Vajtai, R.; Lou, J.; Liu, Z.; Ringe, E. J. A. n., Chemical vapor deposition growth of crystalline monolayer MoSe₂. **2014**, *8* (5), 5125-5131.
22. Bachmatiuk, A.; Abelin, R.; Quang, H. T.; Trzebicka, B.; Eckert, J.; Rummeli, M. H. J. N., Chemical vapor deposition of twisted bilayer and few-layer MoSe₂ over SiO_x substrates. **2014**, *25* (36), 365603.
23. Li, Y.; Wang, F.; Tang, D.; Wei, J.; Li, Y.; Xing, Y.; Zhang, K. J. M. L., Controlled synthesis of highly crystalline CVD-derived monolayer MoSe₂ and shape evolution mechanism. **2018**, *216*, 261-264.
24. Xia, J.; Huang, X.; Liu, L.-Z.; Wang, M.; Wang, L.; Huang, B.; Zhu, D.-D.; Li, J.-J.; Gu, C.-Z.; Meng, X.-M. J. N., CVD synthesis of large-area, highly crystalline MoSe₂ atomic layers on diverse substrates and application to photodetectors. **2014**, *6* (15), 8949-8955.
25. Liu, W.; Liu, M.; OuYang, Y.; Hou, H.; Lei, M.; Wei, Z. J. N., CVD-grown MoSe₂ with high modulation depth for ultrafast mode-locked erbium-doped fiber laser. **2018**, *29* (39), 394002.
26. Utama, M. I. B.; Lu, X.; Zhan, D.; Ha, S. T.; Yuan, Y.; Shen, Z.; Xiong, Q. J. N., Etching-free patterning method for electrical characterization of atomically thin MoSe₂ films grown by chemical vapor deposition. **2014**, *6* (21), 12376-12382.
27. Nam, D.; Lee, J.-U.; Cheong, H. J. S. r., Excitation energy dependent Raman spectrum of MoSe₂. **2015**, *5*, 17113.
28. Jung, C.; Kim, S. M.; Moon, H.; Han, G.; Kwon, J.; Hong, Y. K.; Omkaram, I.; Yoon, Y.; Kim, S.; Park, J. J. S. r., Highly crystalline CVD-grown multilayer MoSe₂ thin film transistor for fast photodetector. **2015**, *5*, 15313.
29. Shim, G. W.; Yoo, K.; Seo, S.-B.; Shin, J.; Jung, D. Y.; Kang, I.-S.; Ahn, C. W.; Cho, B. J.; Choi, S.-Y. J. A. n., Large-area single-layer MoSe₂ and its van der Waals heterostructures. **2014**, *8* (7), 6655-6662.
30. Huang, J.; Liu, H.; Jin, B.; Liu, M.; Zhang, Q.; Luo, L.; Chu, S.; Chu, S.; Peng, R. J. N., Large-area snow-like MoSe₂ monolayers: synthesis, growth mechanism, and efficient electrocatalyst application. **2017**, *28* (27), 275704.

31. Lu, X.; Utama, M. I. B.; Lin, J.; Gong, X.; Zhang, J.; Zhao, Y.; Pantelides, S. T.; Wang, J.; Dong, Z.; Liu, Z. J. N. I., Large-area synthesis of monolayer and few-layer MoSe₂ films on SiO₂ substrates. **2014**, *14* (5), 2419-2425.
32. Chang, Y.-H.; Zhang, W.; Zhu, Y.; Han, Y.; Pu, J.; Chang, J.-K.; Hsu, W.-T.; Huang, J.-K.; Hsu, C.-L.; Chiu, M.-H. J. A. n., Monolayer MoSe₂ grown by chemical vapor deposition for fast photodetection. **2014**, *8* (8), 8582-8590.
33. Tian, X.; Wei, R.; Liu, S.; Zhang, Y.; Qiu, J. J. N., Photoluminescence nonuniformity from self-seeding nuclei in CVD-grown monolayer MoSe₂. **2018**, *10* (2), 752-757.
34. Soubelet, P.; Bruchhausen, A.; Fainstein, A.; Nogajewski, K.; Faugeras, C. J. P. R. B., Resonance effects in the Raman scattering of monolayer and few-layer MoSe₂. **2016**, *93* (15), 155407.
35. Li, Y.; Zhang, K.; Wang, F.; Feng, Y.; Li, Y.; Han, Y.; Tang, D.; Zhang, B. J. A. a. m.; interfaces, Scalable Synthesis of Highly Crystalline MoSe₂ and Its Ambipolar Behavior. **2017**, *9* (41), 36009-36016.
36. Bilgin, I.; Raeliarijaona, A. S.; Lucking, M. C.; Hodge, S. C.; Mohite, A. D.; de Luna Bugallo, A.; Terrones, H.; Kar, S. J. A. n., Resonant Raman and exciton coupling in high-quality single crystals of atomically thin molybdenum diselenide grown by vapor-phase chalcogenization. **2018**, *12* (1), 740-750.
37. Mahjouri-Samani, M.; Liang, L.; Oyedele, A.; Kim, Y.-S.; Tian, M.; Cross, N.; Wang, K.; Lin, M.-W.; Boulesbaa, A.; Rouleau, C. M. J. N. I., Tailoring vacancies far beyond intrinsic levels changes the carrier type and optical response in monolayer MoSe_{2-x} crystals. **2016**, *16* (8), 5213-5220.
38. Kim, K.; Lee, J.-U.; Nam, D.; Cheong, H. J. A. n., Davydov splitting and excitonic resonance effects in Raman spectra of few-layer MoSe₂. **2016**, *10* (8), 8113-8120.
39. Zhao, S.; Tao, L.; Miao, P.; Wang, X.; Liu, Z.; Wang, Y.; Li, B.; Sui, Y.; Wang, Y. J. N. R., Strong room-temperature emission from defect states in CVD-grown WSe₂ nanosheets. **2018**, *11* (7), 3922-3930.
40. Wang, B.; Zhang, Y.; Zhang, H.; Chen, Z.; Xie, X.; Sui, Y.; Li, X.; Yu, G.; Hu, L.; Jin, Z. J. C., Wrinkle-dependent hydrogen etching of chemical vapor deposition-grown graphene domains. **2014**, *70*, 75-80.
41. Cong, C.; Shang, J.; Wu, X.; Cao, B.; Peimyoo, N.; Qiu, C.; Sun, L.; Yu, T. J. A. O. M., Synthesis and optical properties of large-area single-crystalline 2D semiconductor WS₂ monolayer from chemical vapor deposition. **2014**, *2* (2), 131-136.
42. Li, B.; Gong, Y.; Hu, Z.; Brunetto, G.; Yang, Y.; Ye, G.; Zhang, Z.; Lei, S.; Jin, Z.; Bianco, E. J. A. C., Solid-Vapor Reaction Growth of Transition-Metal Dichalcogenide Monolayers. **2016**, *128* (36), 10814-10819.
43. Wu, K.; Li, Z.; Tang, J.; Lv, X.; Wang, H.; Luo, R.; Liu, P.; Qian, L.; Zhang, S.; Yuan, S. J. N. R., Controllable defects implantation in MoS₂ grown by chemical vapor deposition for photoluminescence enhancement. **2018**, *11* (8), 4123-4132.
44. Shi, W.; Lin, M.-L.; Tan, Q.-H.; Qiao, X.-F.; Zhang, J.; Tan, P.-H., Raman and photoluminescence spectra of two-dimensional nanocrystallites of monolayer WS₂ and WSe₂. *2D Materials* **2016**, *3* (2), 025016.
45. Mignuzzi, S.; Pollard, A. J.; Bonini, N.; Brennan, B.; Gilmore, I. S.; Pimenta, M. A.; Richards, D.; Roy, D., Effect of disorder on Raman scattering of single-layer MoS_2 . *Physical Review B* **2015**, *91* (19), 195411.
46. Barker Jr, A.; Sievers, A. J. J. R. o. M. P., Optical studies of the vibrational properties of disordered

solids. **1975**, *47* (S2), S1.

47. Sekine, T.; Izumi, M.; Nakashizu, T.; Uchinokura, K.; Matsuura, E. *J. J. o. t. P. S. o. J.*, Raman scattering and infrared reflectance in 2H-MoSe₂. **1980**, *49* (3), 1069-1077.

48. Doratotaj, D.; Simpson, J. R.; Yan, J.-A. *J. P. R. B.*, Probing the uniaxial strains in MoS₂ using polarized Raman spectroscopy: A first-principles study. **2016**, *93* (7), 075401.

49. Wang, Y.; Cong, C.; Qiu, C.; Yu, T. J. S., Raman spectroscopy study of lattice vibration and crystallographic orientation of monolayer MoS₂ under uniaxial strain. **2013**, *9* (17), 2857-2861.

Supporting Information

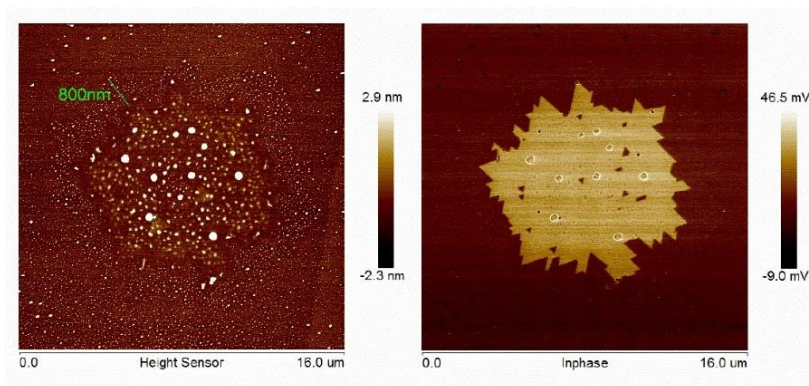


Figure S1. AFM height (left) and phase (right) images of a MoSe₂ monolayer.

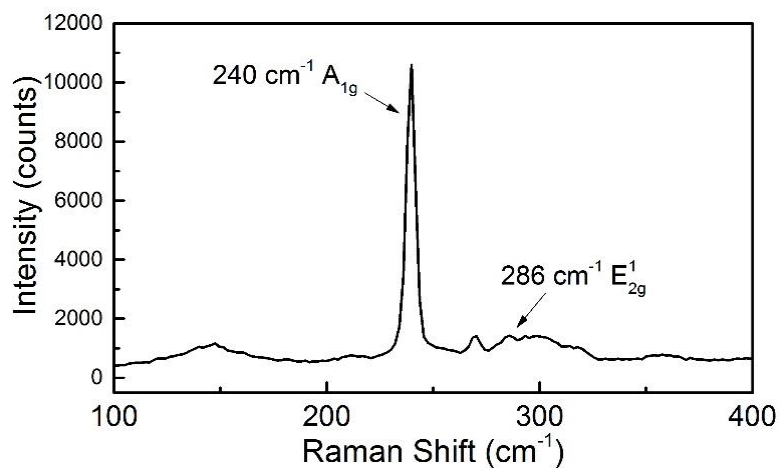


Figure S2 Raman spectrum of monolayer MoSe₂ without Se vacancies

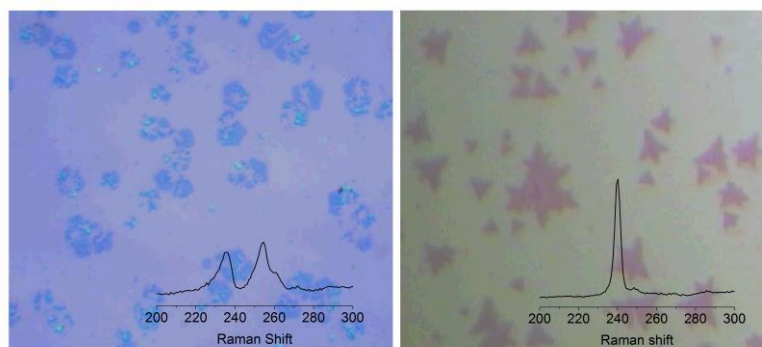


Figure S3 Optical images of MoSe₂ nanosheets at two different Se vacancy concentrations after two months aging. Inserts are the corresponding Raman spectra which can indicate the quality of MoSe₂ nanosheets. Samples in left picture were damaged by air while samples in right remain perfect after two months aging.

DFT calculations for vibrational and Raman properties

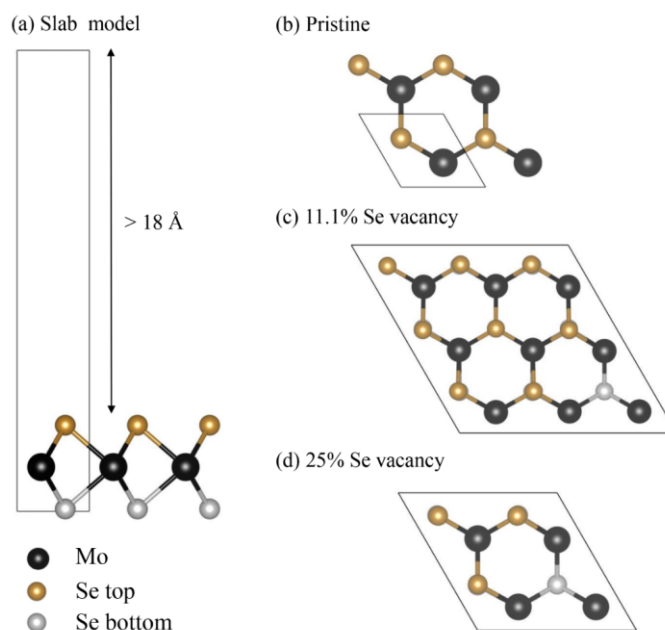


Figure S4. (a) The slab model of 3×3 monolayer MoSe₂. The slab model is extended from the primitive cell. The top views are of (b) pristine, (c) 11.1% V_{Se} , and (d) 25% V_{Se} structures.

To understand the Raman spectrum of defective MoSe₂ films, first-principle density functional theory (DFT) calculation of MoSe₂ monolayer models containing different Se defect concentrations were carried out. Vacuum spacing in the out-of-plane direction is set to be more than 18 Å to avoid spurious interaction. Structure and phonon properties are calculated by Vienna ab initio simulation package (VASP) using the projector-augmented wave (PAW) methods and Perdew-Burke-Ernzerhof (PBE) functional with D3 correction (DFT-D3). The energy cutoff was set as 400 eV and residual forces for ion iteration as 10^{-4} eV/Å.

The vacancy concentration is defined as the number of Se vacancy sites divided by the total number of Se atoms in the defective Se layer. We have considered models of three Se defect concentrations: pristine, 11.1% (3×3 supercell with a single Se vacancy) and 25% (2×2 supercell with a single Se vacancy), as shown in Figure S3. For a primitive unit cell of pristine MoSe₂, it was optimized with Γ -centered $24 \times 24 \times 1$ Monkhorst-Pack (MP) k-points and the optimized in-plane lattice constant is 3.29 Å. The Γ -centered MP grids were set as $12 \times 12 \times 1$ and $16 \times 16 \times 1$ for 11.1% defective model and 25% defective model respectively.

After the structural relaxations, the normal vibration modes are calculated within frozen phonon approximation. Given these vibration mode, Raman tensors and intensities are obtained based on the calculation of the derivatives of the dielectric tensors with respect to phonon vibration using the script “vasp_raman.py”^[1]. This is a Raman off-resonant activity calculator using VASP as a back end. Lorentz broadening of the modes’ intensities yielded the Raman spectrum.

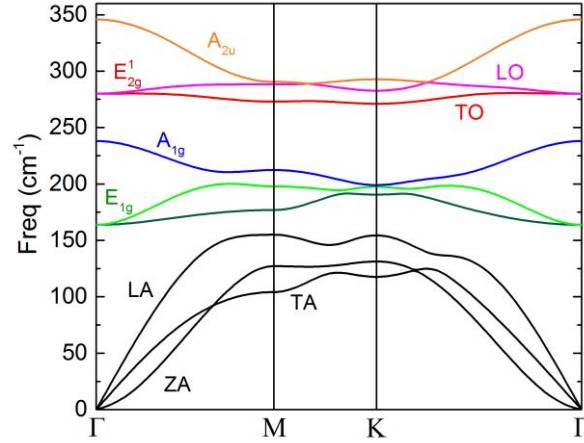


Figure S5 Calculated Phonon dispersion of monolayer MoSe₂

Polarized Raman scattering

As shown in Figure S6 the polarization direction of scattered light's electric field is fixed in an arbitrary angle, θ , to x axis. The induced angle, ϕ , between the polarization directions of incident light and scattered light is tuned from 0° to 360°. The Raman intensity for a given configuration can be determined by Raman tensor^[2]:

$$I \propto |\hat{g}_s \cdot \tilde{R} \cdot \hat{g}_i|^2$$

where \tilde{R} is the Raman tensor of the Raman mode, $g_s = (\cos \theta, \sin \theta)$, $\hat{g}_i = (\cos(\theta + \phi), \sin(\theta + \phi))$.

According to the Raman tensors given in the main article, the intensities of A_{1g} mode and D mode are both proportional to $\cos^2 \phi$, consistent with our experimental results shown in Figure 6d. Cross and parallel configurations mean that ϕ is 90° and 0° respectively.

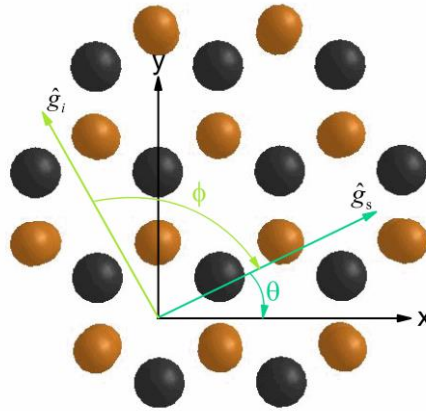


Figure S6. The diagram of Polarized Raman scattering experiments in Cartesian coordinate systems. \hat{g}_s is the direction of scattered light and \hat{g}_i is the direction of incident light. x- and y-directions represent zigzag and armchair directions respectively.

X-ray photoelectron spectroscopy analysis

The X-ray photoelectron spectroscopy (XPS) was adopted to determine the Se/Mo ratio in MoSe₂ samples with different Se vacancy concentrations. As seen in Figure S7, the doublet of Mo⁴⁺ core levels are located at 229.1 eV (3d_{5/2}) and 232.2 eV (3d_{3/2}), and doublet of Se²⁻ 3d core levels are located at 54.4 eV (3d_{5/2}) and 55.4 eV (3d_{3/2}). The difference value (~174.7 eV) between the 3d_{5/2} peaks of Mo⁴⁺ and Se²⁻ confirms the Mo-Se bond.^[3] It should be noted that the 3d peak of Mo⁶⁺ and 3s peak of Se²⁻ have an overlap with 3d peak of Mo⁴⁺.^[4] MoO₃ nanoparticles arising from the raw material should be responsible for the Mo⁶⁺ peak in XPS, which can be identified by AFM image in Figure S1. Se/Mo ratios are estimated by the ratios of peak areas of Mo⁴⁺ (3d) and Se²⁻ (3d) concerning the element sensitivity factors (1.6 for Se, 11.008 for Mo).^[5]

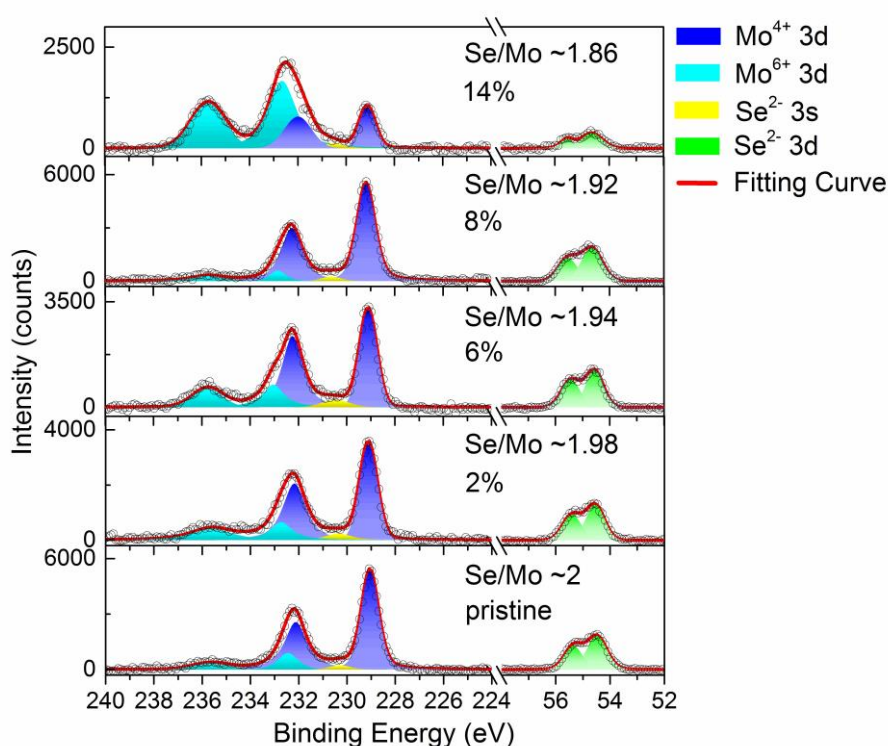


Figure S7. XPS spectra of MoSe₂ samples with different Se vacancy concentrations.

Reference:

- [1] A. Fonari and S. Stauffer, vasp_raman.py [<https://github.com/raman-sc/VASP/>] (retrieved 2013)]
- [2] Doratotaj, D.; Simpson, J. R.; Yan, J.-A. *Physical Review B* 2016, 93, (7).
- [3] J. C. Bernede, J. P., and Z. K. Alaoui. *Applied Physics A* 1990, 51, 155-159.
- [4] Krbal, M.; Prikryl, J.; Zazpe, R.; Dvorak, F.; Bures, F.; Macak, J. M. *physica status solidi (RRL)-Rapid Research Letters* 2018, 12, (5).
- [5] Wagner, C. D. *Journal of Electron Spectroscopy and Related Phenomena* 1983, 32, 99-102.